MATERIALS SCIENCE & ENGINEERING A

ELSEVIER

Grid indentation analysis of composite microstructure and mechanics: Principles and validation

G. Constantinides [a], K.S. Ravi Chandran [c], F.-J. Ulm [a], K.J. Van Vliet [b,*]

[a] *Department of Civil and Environmental Engineering, Massachusetts Institute of Technology, Cambridge, MA 02139, USA*
[b] *Department of Materials Science and Engineering, Massachusetts Institute of Technology, Cambridge, MA 02139, USA*
[c] *Department of Metallurgical Engineering, The University of Utah, Salt Lake City, UT 84112-0114, USA*

Abstract

Several composites comprise material phases that cannot be recapitulated *ex situ*, including calcium silicate hydrates in cementitous materials, hydroxyapatite in bone, and clay agglomerates in geomaterials. This requirement for *in situ* synthesis and characterization of chemically complex phases obviates conventional mechanical testing of large specimens representative of these material components. Current advances in experimental micro and nanomechanics have afforded new opportunities to explore and understand the effect of thermochemical environments on the microstructural and mechanical characteristics of naturally occurring material composites. Here, we propose a straightforward application of instrumented indentation to extract the *in situ* elastic properties of individual components and to image the connectivity among these phases in composites. This approach relies on a large array of nano to microscale contact experiments and the statistical analysis of the resulting data. Provided that the maximum indentation depth is chosen carefully, this method has the potential of extracting elastic properties of the indented phase which are minimally affected by the surrounding medium. An estimate of the limiting indentation depth is provided by asssuming a layered, thin film geometry. The proposed methodology is tested on a "model" composite material, a titanium-titanium monoboride (Ti–TiB) of various volumetric proportions. The elastic properties, volume fractions, and morphological arrangement of the two phases are recovered. These results demonstrate the information required for any micromechanical model that would predict composition-based mechanical performance of a given composite material.
© 2006 Elsevier B.V. All rights reserved.

Keywords: Indentation analysis; Composites; Titanium-titanium boride; Material characterization

1. Introduction

The mechanically significant phases of several composites, including calcium silicates in cementitious materials, hydroxyapatite in bones, and clay agglomerates in geomaterials, cannot be adequately reproduced *ex situ* in large specimens. This restricts the use of conventional mechanical characterization approaches such as uniaxial tension/compression or resonance frequency. As a consequence, the intrinsic (and thermochemically altered) mechanical properties of such phases are essentially unknown. The advent of instrumented indentation [14,40] provides an unprecedented opportunity to measure the mechanical response of these phases at the appropriate length scale ($\sim 10^{-6}$ m). Such data is a critical requirement of multiscale mechanical modeling

efforts that would predict the composite mechanical performance for a given composition and microstructure.

It is now well established that the response of a material upon the reversal of contact loading provides access to the elastic properties of the indented material (for recent reviews see Refs. [6,31]). The indentation technique consists of establishing contact between an indenter of known geometry and mechanical properties (typically diamond) and the indented material for which the mechanical properties are of interest, and subsequently acquiring the continuous change in penetration depth h as a function of increasing indentation load P (P–h curve). Typically, the extraction of properties is achieved by applying a continuum scale mechanical model to derive two quantities, indentation hardness H and indentation modulus mechanical M [2,11,30,39]:

$$H \overset{\text{def}}{=} P/A_c \tag{1a}$$

* Corresponding author. Tel.: +1 617 25 3315; fax: +1 617 253 8745.
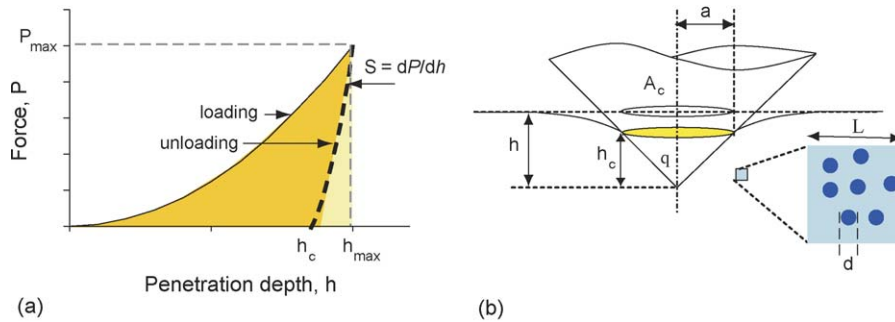 *E-mail address:* krystyn@mit.edu (K.J. Van Vliet).

Fig. 1. Principles of indentation testing.

$$M \stackrel{\text{def}}{=} \frac{\sqrt{\pi}}{2} \frac{S}{\sqrt{A_c}} \tag{1b}$$

All quantities required to determine H and M are directly obtained from the P–h curves, with the exception of the projected area of contact A_c. Chief among these are the maximum applied force P_{max} and corresponding maximum depth h_{max}, the unloading indentation stiffness $S = \frac{dP}{dh}|_{h=h_{max}}$, and residual indentation depth h_f upon full unloading of the material surface (Fig. 1). The contact area A_c can also be extrapolated from the maximum depth h_{max} [17,30,31]. Furthermore, M can be linked to the elastic modulus E of the indented material by applying a linear elastic model to the data [15,36]. The methodology however, is currently restricted to monolithic systems, and little has been reported for indentation on composite materials, a category composing the majority of solids. Application of Eqs. (1a) and (1b) to multiscale composites poses several difficulties, as the underlying analysis relies on the self-similarity of the indentation test; this strictly holds only for homogeneous materials [3].

Herein, we explore the following question: is it possible to apply continuum indentation analysis to structurally heterogeneous materials and, if so, how? We propose a straightforward extension of instrumented indentation analysis for multiscale composites, which by design circumvents the interaction between the individual phases present in the microstructure. In particular, we present a grid indentation technique that, under certain restrictions, can provide both quantitative and qualitative information about the morphology and mechanical properties of individual phases comprising the material. The large amount of data acquired is treated in a statistical sense. That is, statistical analysis of results provides access to the mechanical properties and volumetric proportions of all phases comprising the material, and additionally the spatial representation of mechanically distinct phases elucidates the morphological arrangement of different phases. This is illustrated here for Berkovich indentation in a "model" binary composite material: titanium-titanium boride (Ti–TiB).

2. Identifying critical length scales: thin film analogy

The literature on indentation on composite materials includes only few very recent publications [8,9,12,19,25]. This limited activity is not altogether surprising, given the complexity of the mechanical response of a material system when indentation vol-umes and microstructural volumes are of the same order (see Fig. 1). This lack of length scale separation obfuscates the use of continuum analysis to translate indentation data into meaningful mechanical properties. We therefore propose a means to reduce this complexity through careful choice of indentation length scales that enable application of continuum indentation analysis.

2.1. Indentation length scales

Continuum indentation analysis is premised on spatially homogeneous mechanical response and, therefore, constitutive relations between stress and strain that are independent of the length scales of analysis such as the indentation depth h [3]. The representative volume element (RVE) of homogeneous mechanical response and characteristic size $\mathcal{L}$ must obey to the length scale separability condition:

$$d \ll \mathcal{L} \ll (h, a, D) \tag{2}$$

where (h, a) are the indentation depth and the indentation radius, respectively, that define the order of magnitude of the variation of the position vector $\underline{x}$, D is a characteristic microstructural length scale, and d is the characteristic size of the (largest) microstructural/mechanical heterogeneity contained in the RVE. Provided that Eq. (2) is satisfied, an indentation experiment executed to an indentation depth h gives access to the material properties that are characteristic of the material at a length scale of $\mathcal{L}$ (see Fig. 1). Most indentation solutions are based on the self-similarity approach, derived from the infinite half-space model (which by definition has no length scale limit) that assumes spatially uniform mechanical properties (see e.g., Ref. [6]). Therefore, the properties extracted by means of an inverse analysis from indentation data are averaged quantities characteristic of a material length scale defined by the indentation depth h or the indentation radius a. A good estimate is that the characteristic size of the material domain sensed by an indentation is of the order of $\max(h, a)$; roughly $3h$ for Berkovich indentation and h for the corner cube. Given the self-similarity of the indentation contact, the choice of indentation depth directly determines the length scale of the material RVE. Analysis of composite materials requires consideration of the case in which the microstructural length D is of the order of the indentation depth h, for which the classical tools of continuum indentation analysis would not apply.

2.2. Intrinsic phase properties: $h \ll D$

We thus aim to derive a critical indentation depth below which microstructural length scales do not interfere significantly with the indentation response, such that indentation data acquired to such a depth provide access to the intrinsic properties of the material comprising that RVE of the microstructure. The simplest geometrical representation of a heterogeneous binary (two-phase) composite system is a layered medium, which is in fact the most severe geometric heterogeneity that can be investigated via indentation [12]. Such layered systems have been investigated in some detail in the context of thin films on substrates, one of the most popular current applications of nanoindentation. In the case of this thin film analogy, we equate film thickness t with the characteristic length scale of the microstructure D in Eq. (2), and explore thin film indentation models to identify a critical indentation depth below which the properties of the homogeneous phase are measured accurately. We restrict our analysis here to the indentation stiffness, film stiffness E_f, but similar concepts can be extended to the film hardness H_f.

The majority of models for thin film indentation rely on phenomenological arguments or finite element simulations, and tend to relate the composite modulus E_{eff} to the elastic moduli of the film E_f and of the substrate E_s:

$$E_{eff} = E_f + (E_s - E_f)\Psi \tag{3}$$

where Ψ is a weight function that depends on the ratio of indentation depth to film thickness h/t. In fact, as $\Psi \to 0$, the effect of the substrate is eliminated and $E_{eff} \to E_f$. Several models have been proposed in the literature to estimate Ψ and quantify the effect of the substrate on the composite response. By using the Hankel's transform method, Li and Chou [26] calculated the Green's function for a coated substrate and evaluated the displacement, stress field and load–indentation depth relation of the thin film/substrate system under an axisymmetrically distributed contact load. King [24] studied the effect of the substrate on the global response using finite element simulations, whereas Gao et al. [16] devised a first-order rigorous moduli-perturbation method to derive a closed-form solution for the contact compliance of an uncracked film/substrate composite:

$$\Phi^G = 1 - \Psi^G = \frac{2}{\pi} \tan^{-1}\left(\frac{t}{a}\right)$$
$$+ \left[(1 - 2\nu)\left(\frac{t}{a}\right) \ln\left(\frac{1 + (t/a)^2}{(t/a)^2}\right) - \frac{(t/a)}{1 + (t/a)^2} \right]$$
$$\times [2\pi(1 - \nu)]^{-1} \tag{4}$$

In this approach, based on a perturbation calculation of the elastic energy of a coated substrate indented with a flat punch of radius a, the assumption is made that the mechanical properties of both materials do not differ widely. The model was validated by Chen and Vlassak [5] by means of finite element analysis, showing that the model is correct for moduli mismatch ratio in the range 0.5–2, deviating from reality in cases when the contrast is higher. Yu et al. [42] have considered the elastic solution of an axisymmetric mixed boundary value problem and the results (for spherical, conical, or cylindrical flat punch contact) are obtained

by solving a Fredholm integral equation of the second kind with a continuous symmetrical kernel which depends on the bonding conditions. With the aid of finite element calculations, Chen and Vlassak [5] compared the theoretical results of Yu et al. [42] with numerical results and showed very good agreement. Perriot and Barthel [32] proposed a method relying on the work by Li and Chou [26], in which they calculated the Green's function for a coated substrate. The stress/strain relation of Li and Chou could not be inverted and thus not implemented easily for contact problems. Using the auxiliary fields introduced by Sneddon and Ting [37,41], however, Perriot and Barthel have reformulated this solution to allow inversion, and have found that the load–displacement response is independent of indenter geometry and modulus mismatch. This response is very much like that provided by Gao et al. [16], and is also in good agreement for the modulus mismatch ratio in the range 0.5–2. Perriot and Barthel have empirically extended Eq. (4) to a wider range of modulus mismatch ratios ($E_s/E_f = 0.01$–100):

$$\Psi^{PB} = \left[1 + \left(\frac{t}{a}k\right)^n \right]^{-1} \tag{5}$$

where a is the contact radius, n is an empirical constant ($n \sim 1.27$) and k is defined by:

$$\log(k) = -0.093 + 0.792 \log\left(\frac{E_s}{E_f}\right) + 0.05\left(\log\left(\frac{E_s}{E_f}\right)\right)^2 \tag{6}$$

Eqs. (3) to (6) show a fair degree of consistency and suggest that substrate effects are negligible for stiffness mismatch ratio $E_s/E_f \in [0.2, 5]$ as long as the indentation depth h (or contact radius a) is smaller than or equal to 10% of the film thickness t. This is illustrated in Fig. 2 in which the critical a/t-ratio, $(a/t)_{10\%}$, for which the error in the modulus estimation, $(E_{eff} - E_f)/E_f$, does not exceed $\pm 10\%$, is shown as a function of the modulus mismatch ratio E_s/E_f.
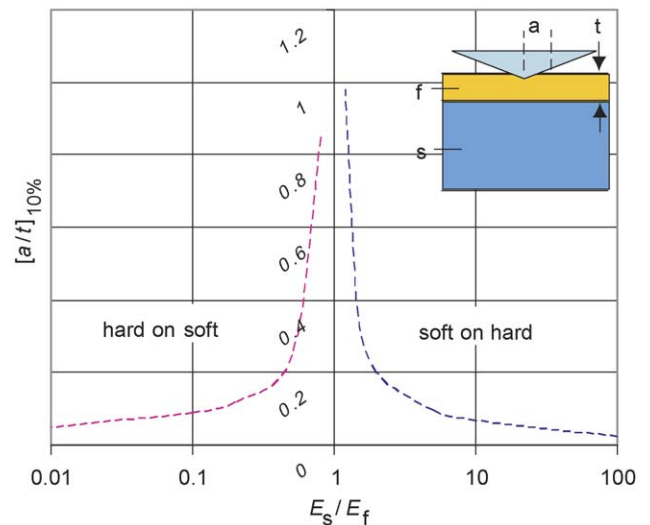

Fig. 2. Critical a/t-ratio vs. E_s/E_f as predicted by Perriot and Barthel [32] for which the composite modulus, E_{eff}, is within 10% of the film modulus, E_f. a is the contact radius and t is the thickness of the layer.

The above models have been developed for a very specific geometric arrangement of two phases, but are generally considered to be a very good first-order approximation for more general morphologies. The only available information for particulate systems in the literature is a finite element study by Durst et al. [12], who performed numerical investigations of hardness for overlaying-substrate systems having a yield strength ratio of 0.5–2. Three different geometries are considered: a layered medium, a square particle embedded in a semi-infinite medium, and a semi- infinite fiber embedded in an semi-infinite medium. These results suggest that the thin film geometry yields the most severe restrictions on the depth of indentation and, therefore, use of the thin-film analogy to define a critical indentation depth with respect to the size of the heterogeneity appears to be a conservative choice.

In summary, in order to apply continuum indentation analysis to heterogeneous systems, the indentation depth should be at most 1/10 of the characteristic size of the microstructure D in order to access phase properties. This rule of thumb, also known as 1/10-rule of Buckle [4], is a rough first estimate and in cases where the contrast between the mechanical properties of the two phases becomes significant (($\frac{E_s}{E_f}$) $\notin$ [0.2, 5]) the method tends to be too relaxed – at higher indentation depths, the indentation response interferes with microstructure, and special care should be taken in the interpretation of the indentation results.

2.3. Composite properties: $h \gg D$

To complete the thin film analogy, it is useful to provide an estimate for the indentation depth that gives access to composite properties. The finite element simulations of Durst et al. [12] suggest that the response reaches an asymptotic values for $a/t > 2$. Equating t with D, it is possible to estimate that an indentation depth of $h > 2D \cot \theta$ (with θ the equivalent cone semi-angle; see Fig. 1) should give access to composite material properties. Hence, it is at indentation depths h between these two limiting cases, $0.01 < h/D < 2 \cot \theta$ that microstructure is expected to strongly affect the measured indentation response.

3. Massive array indentation experiments

3.1. Gedanken experiment

Consider a material to be composed of two phases of different mechanical properties and characterized by a length scale D. If the indentation depth is much smaller than the characteristic size of the phases, $h \ll D$ (Section 2.2) then a single indentation test gives access to the material properties of either phase 1 or phase 2. If, in addition, a large number of tests ($N \gg 1$) are carried out on a grid (Fig. 3) defined by a grid spacing ℓ that is larger than the characteristic size of the indentation impression, so to avoid interference in between individual indentation tests, and much larger than the characteristic size of the two phases ($\ell\sqrt{N} \gg D$), so that the locus of indentation has no statistical bias with respect to the spatial distribution of the two phases,
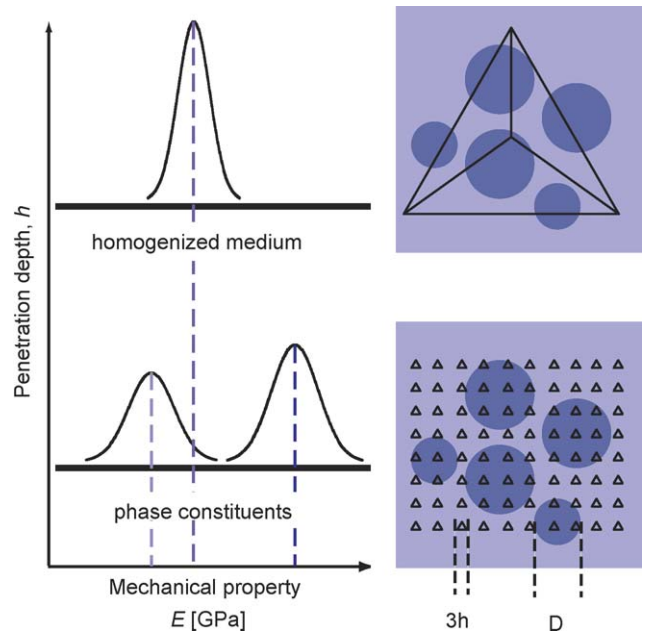

Fig. 3. Schematic of the principle of the proposed massive array or grid indentation technique for heterogeneous materials. Bottom: at low indentation depths ($h \ll d$) the individual constituents can be identified giving rise to multimode ditributions. Top: at large indentation depths ($h \gg d$) the properties of a homogenized medium are obtained.

the probability of encountering one or the other phase is equal to the surface fraction occupied by the two phases on the indentation surface. Provided that a similar distribution is found equally on other surfaces, the surface fraction can be assimilated with the volume fraction of the two phases present in the (isotropic) material. Consider next an indentation test performed to a maximum indentation depth that is much larger than the characteristic size of the individual phases, $h \gg D$ (Section 2.3). It is readily understood, by letting $D = d$ in the scale separability condition of Eq. (2), that the properties extracted from such an indentation experiment are representative in a statistical sense of the average properties of the composite material.

This simple gedanken experiment has all the ingredients of statistical indentation analysis that need to be performed when it comes to composite materials. The key results of such analysis are distributions and their derivatives (e.g., histograms or frequency diagrams) of mechanical properties determined by a large number of indentation experiments at a specific scale of material observation defined by the indentation depth. Generally speaking, small indentation depths ($h < 0.1D$) provide access to mechanical phase properties, and potentially to volume fractions:

$$f_J = \frac{N_J}{N}; \qquad \sum_{J=1}^{n} N_J = N \qquad (7)$$

where N_J is the number of indentations on material phase J, that can be identified by the difference in material properties; that is f_J is the volume fraction of a mechanically distinct material phase. In turn, greater indentation depths ($h > 2D \cot \theta$) provide access to homogenized material properties of the composite. This principle is demonstrated in Fig. 3. Finally, a mapping of

mechanical properties allows one to identify characteristic morphologies within the resolution defined by the array spacing.

3.2. Deconvolution of mechanical response distributions

The above gedanken experiment is based on the premise that the two phases have two properties of sufficient contrast that these can be separated in small-scale indentation tests. Composite materials are generally more complex, requiring the use of some elementary statistics relations to analyze the indentation data. Let us assume that the distribution of the mechanical property $x = M$ of each phase J is best approximated by the normal or Gaussian distribution:

$$p_J(x) = \frac{1}{\sqrt{2\pi s_J^2}} \exp\left(-\frac{(x - \mu_J)^2}{2s_J^2}\right) \tag{8}$$

where the mean μ_J is the arithmetic mean of all N_J values of each phase, while the standard deviation, s_J, or the root mean square deviation, is a measure of the dispersion of these values:

$$\mu_J = \frac{1}{N_J} \sum_{k=1}^{N_J} x_k; \qquad s_J^2 = \frac{1}{N_J - 1} \sum_{k=1}^{N_J} (x_k - \mu_J)^2 \tag{9}$$

The case of a single phase, $n = 1$, corresponds to the case of a homogenous material, for which mean value and standard deviation describe the properties of the material in a statistical sense. In the case of several phases ($J = 1, n$), that all follow a normal distribution, and which do not (mechanically) interact with each other, the overall frequency distribution of the mechanical property $x = M$ obeys to the following theoretical probability density function:

$$P(x) = \sum_{J=1}^{n} f_J \, p_J(x) \tag{10}$$

where f_J is the volume fraction of phase J subjected to the constraint:

$$\sum_{J=1}^{n} f_J = 1 \tag{11}$$

Hence, there is a total of $3n - 1$ unknowns in the problem of Eq. (10); (f_J, μ_J, s_J) for each phase reduced by the compatibility condition of Eq. (11). If empirical frequency densities or response distributions are obtained by nanoindentation in form of discrete values P^i one can determine the unknowns by minimizing the standard error:

$$\min \sum_{i=1}^{m} \frac{(P^i - P(x_i))^2}{m} \tag{12}$$

where P^i is the observed value of the experimental frequency density, $P(x_i) = \sum_{J=1}^{n} f_J \, p_J(x_i)$ is the value of the theoretical probability density function shown in Eq. (10) at point x_i, and m is the number of intervals (bins) chosen to construct the histogram. The number of observed values P^i should exceed the number of unknowns, and will obviously be smaller than the total number of experiments; hence:

$$3n - 1 \leq m < N \tag{13}$$

In the application of the deconvolution technique to composites, the number of phases n is generally known in advance. Indeed, in small-scale indentation ($h \ll D$) n is determined by the number of distinct chemical phases (e.g., those identified by X-ray diffraction) and/or morphological units (e.g., those identified by optical or electron microscopy) that comprise the microstructure. In turn, for the large-scale indentation response ($h \gg D$), $n = 1$ represents the composite material.

4. Experimental validation of massive array indentation

To validate the proposed approach, we have investigated a series of discontinuously reinforced titanium alloys containing titanium boride (TiB) whiskers in different distributions. The microstructural evolution and the volume fractions of the different phases have been studied in detail in Refs. [34] and [1], respectively. Titanium-titanium monoboride alloys (Ti–TiB) are currently considered as possible candidate materials for several advanced applications, ranging from military and aerospace applications to automobile parts. Other attractive reinforcing materials like SiC, C, or Al_2O_3 lead to the formation of reaction products at the interface, which have hindered macroscopic mechanical performance. The TiB particle reinforcement was found to circumvent the problems associated with reactivity of titanium [13,35], while maintaining the advantages of a metal matrix composite (MMC) including improved specific strength, creep, and corrosion resistance as compared to the titanium alloy matrix. While TiB currently serves as reinforcement in many MMCs, the elastic properties of this phase are essentially unknown. Similarly to calcium silicate hydrates in cement-based composites or clay minerals in geomaterials, the TiB phase cannot be adequately reproduced in large specimens required of traditional testing methods. The proposed grid indentation approach provides a unique opportunity to measure the elastic response of single crystal TiB at length scales of the order of the phase diameter, and additionally to validate the generality of the proposed experimental approach. The extracted results will be used as input information in a micromechanical model that provide predictions about the elastic composite response, and then compared with published macroscopic elasticity measurements.

4.1. Materials and methods

4.1.1. Specimen preparation

Ti–TiB composites of varying volume fractions were made by reaction sintering of Ti and TiB_2 powder compacts under pressure in a hot press in an Argon back-filled atmosphere. Commercially available Ti powder (source: Alfa Aesar, War Hall, MA) of average particle size: 28 μm and composition in wt.%: 0.23% O, 0.02% N, 0.01% C, 0.04% Fe, and 0.024% H was used. The TiB_2 powder (source: Advanced Ceramics Corporation, Cleveland, OH) of average particle size: 2.4 μm and composition in wt.%: 30.3% B, 0.67% Zr, 0.01% C, 0.04% Fe, and 0.024% H was used as the source of B. The mixtures were

Table 1
Volumetric proportions of power mixture and resulting composite solid composition

Powder mixture (%)	Composite (%)		
Ti/TiB$_2$	Ti	TiB	TiB$_2$
1.000/0.000	1.00	0.00	0.00
0.882/0.118	0.70	0.30	0.00
0.763/0.237	0.45	0.55	0.00
0.408/0.592	0.00	0.92	0.08

prepared by mixing and ball milling to produce the target compositions of 0.0, 0.2, 0.6, and 1.0 volume fractions of TiB in the Ti–TiB composites. Table 1 lists the powder mixture proportions and the resulting volume fractions of Ti, TiB and TiB$_2$ phases in the composite. TiB is an intermediate phase between Ti and TiB$_2$ components in the Ti–B phase diagram and the formation of TiB proceeds by the simple reaction:

$$Ti + TiB_2 \rightarrow 2TiB \qquad (14)$$

Reaction sintering was carried out at temperatures ranging from 1100 to 1400 °C under varying levels of pressures for different compositions, to yield completely reacted and transformed microstructures in the final compacts. Density measurements and optical microscopic observations assured the full density of the composites. Samples of size of about 10 mm × 10 mm × 3 mm were cut by electro-discharge-machining (EDM) from the fabricated plates. The samples were ground and successively polished with 125-, 75-, 40-, 20-, and 10-μm metal-bonded diamond disks. Final polishing was carried out with 6-, 1-, and 0.1-μm diamond pastes on a felt cloth. The samples were then etched with Kroll's reagent. Microstructural examination was conducted in a Hitachi 3000N scanning electron microscope (SEM) in secondary electron imaging mode. Some samples, especially the high TiB volume fraction composites were repetitively etched to reveal the extremely fine TiB whisker bundles. X-ray diffraction analyses were carried out on polished specimens in a Siemens D5000 X-ray diffractometer operated at 40 kV and 40 mA and using Cu Kα radiation. High resolution scans were made to determine accurately the integrated intensities of specific diffraction peaks. The intensity profiles were then Gaussian-fitted to estimate the volume fractions of phases.

4.1.2. Ti–TiB composite microstructural characteristics

The TiB whiskers formed by *in situ* reaction in the composites had a variety of sizes and aspect ratios that also varied with the volume fraction of TiB itself (see Fig. 4). This is due to the nature of powder packing, sintering times and the amount of TiB$_2$ that was required to form a composite of TiB in equilibrium with Ti at the process temperature. Nevertheless, in all composites, TiB invariably formed as whiskers of varying aspect ratios. The 70%Ti–30%TiB composite consisted of long, needle shaped TiB whiskers with a maximum length of about 50 μm and a width of about 5 μm embedded in Ti matrix. Duplex TiB whisker structure was observed in 45%Ti–55%TiB composite; the first being needle-shaped and long TiB whiskers of about 40 μm in length and about 4 μm in width, randomly oriented in Ti matrix, and the second being bundles of short TiB whiskers of about 1.4 μm
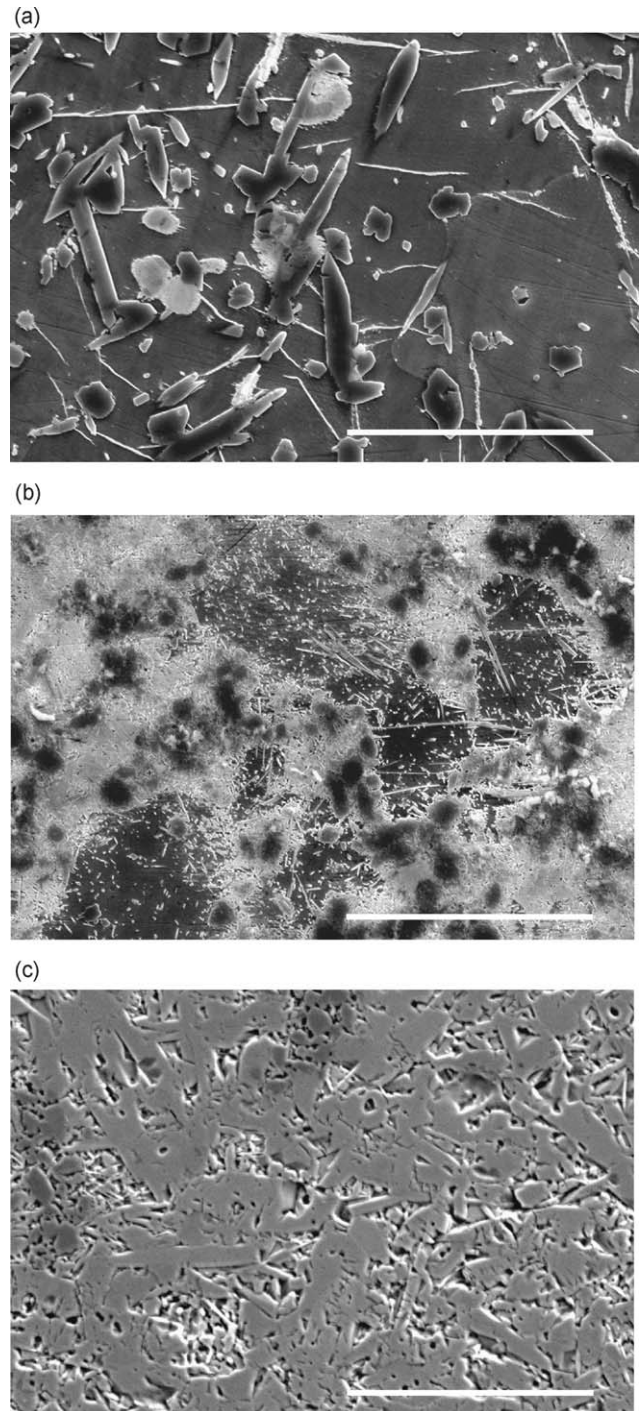

Fig. 4. Scanning electron microscopy images of etched Ti–TiB–TiB$_2$ specimens: (a) 70%Ti–30%TiB, (b) 45%Ti–55%TiB, (c) 92%TiB–8%TiB$_2$. Scalebars = 50 μm.

in length and about 0.6 μm in width, containing traces of Ti in between them. The pronounced refinement in these compositions relative to the other compositions has been explained (see Ref. [34]) on the basis of powder packing, anisotropic diffusion of B in TiB and the mean-free-path length available for TiB whisker growth in a given powder-packed configuration. The TiB phase coarsened significantly and lost the whisker structure in the 92%TiB–8% TiB$_2$ composite – the average length of TiB

Table 2
Experimental program and mean ± standard deviation of indentation results

	100Ti	70Ti–30TiB	45Ti–55TiB	8Ti–86TiB–6TiB$_2$
#	1×100	2×100	2×100	2×100
P^*_{max} (μN)	3481 ± 2	3484 ± 2	493 ± 2	3495 ± 1
h_{max} (nm)	179 ± 18	137 ± 33	40 ± 11	89 ± 8
S (μN/nm)	79.94 ± 10.38	81.69 ± 55.82	47.11 ± 5.52	142.25 ± 7.36
$\tau_L/\tau_H/\tau_U$ (s)	10/5/10	10/5/10	10/5/10	10/5/10

 * The deviation of the maximum force from the applied number is due to the spring force correction (see Ref. [22]).

phase was about 20 μm and the width was about 4 μm. The solid solubility of B in Ti at room temperature is practically negligible and all the B is present in the form of either TiB or TiB$_2$.

4.1.3. Indentation parameters

We have suggested that the elastic properties of the individual components can be accessed by indentation experiments with maximum indentation depths $h_{max}/D \leq 1/10$.[1] In nanoindentation, the maximum indentation depth must be such that the scale separability condition of Eq. (2) is satisfied:

$$d_0 \ll h_{max} \leq D/10. \qquad (15)$$

Hence, in order to obtain the properties of Ti and TiB, d_0 and D represent the characteristic sizes of, respectively, the heterogeneity within Ti and TiB, and D the microstructure of TiB. The crystalline nature of titanium and titanium boride imply d_0 of the order the lattice parameters of the underlying crystal structures (Angstroms). Certainly, the characteristic size of the microstructure D is more difficult to estimate, as the size and shape of the TiB whiskers depend directly on initial composition and heat treatment (temperature, duration, etc.). Scanning electron microscopy images of Ti–TiB [18,34] suggest that a length scale of $D_I \sim 1 - 3$ μm is characteristic of the TiB whiskers (see Fig. 4); we adopt this limit herein. Hence, an appropriate indentation depth that allows access to the Ti and TiB phases by nanoindentation is:

$$h_{max} \in [100, 300]\,\text{nm} \qquad (16)$$

In the case of 45%Ti–55%TiB specimen, the TiB whiskers exhibited a refined morphology and the indentation depth was reduced further to access the individual constituents, $h_{max} \simeq 40$ nm. For smaller depths, issues related to imperfect geometry at the indenter apex may become significant [14], and for larger depths the "substrate effect" related to the proximity of other phases will prohibit access to intrinsic properties of the TiB. We should emphasize, however, that Eq. (15) is only satisfied in an average sense, and that the presence of experiments within an array that violate these conditions is inevitable. For instance, the length and width of TiB whiskers has been determined previously to vary within a specimen (especially for 45%Ti–55%TiB), with a fraction of the whisker population exhibiting widths $D < 1$ μm [18]. The error induced by indentation on such

phases that do not satisfy Eq. (15) is expected to be random in nature, and should be captured by the statistical analysis method (see Section 3.2).

Finally, we must relate the target indentation depths to the massive array of experiments conducted on a highly heterogeneous material (see Fig. 3). A convenient way to achieve on-average indentation depths of the magnitude specified by Eq. (16) is to employ a series of load-controlled indentation experiments. This requires some experimental iteration. For the present material system, we found that a maximum load of $P_{max} = 3500$ μN yields an average maximum indentation depth of $h_{max} \in [60, 100]$ nm. Experiments were conducted using a commercial nanoindenter (Hysitron, Inc. TriboIndenter) that applies load and acquires load and displacement via a single capacitive transducer and initiates contact with the sample surface via piezoactuation of this transducer. In all indentation experiments a trapezoidal load history was prescribed, defined by a loading segment duration $\tau_L = 10$ s, a holding period at P_{max} of $\tau_H = 5$ s, and an unloading segment duration $\tau_U = 10$ s. In addition, a holding period of 10 s subsequent to the initiation of contact facilitated correction for thermal drift within the load train of the instrumented indenter. Table 2 summarizes the details of the experimental program.

4.2. Indentation results and statistical analysis

Indentation results were analyzed both individually and globally: An individual test gives access to mechanical information of the indented region, and a series of tests describes the composite material behavior. Typical load–depth ($P - h$) responses for indentation on the two phases (Ti and TiB) are illustrated in Fig. 5. The complete set of indentations varied in terms of the maximum indentation depths all across the region defined by these two extreme scenarios, depending on the degree of interaction between the two phases. The majority of the responses, however, were centered around these two mean values. This will be further exemplified through the statistical analysis of the indentation moduli presented below. Individual tests were analyzed based on the methodology presented by Oliver and Pharr [30]: a function of the form $P = b(h - h_f)^m$ was fitted to the unloading portion of the P–h curve and the indentation stiffness, S, was evaluated at maximum load, P_{max}. The indentation modulus, M, was then calculated from Eq. (1b), where the area of contact at maximum load, A_c, was estimated according to the area function approach of Oliver and Pharr. This method is based on the assumption that the elastic contact height-to-indentation depth relation [36], $h_c/h = 2/\pi$ equally applies to the elastic recovery

---

[1] We recall that the critical indentation depth would be a function of the moduli mismatch E_s/E_f. For general composites where the modulus E_f is unknown $h_{max}/D \leq 1/10$ would be a good starting point.
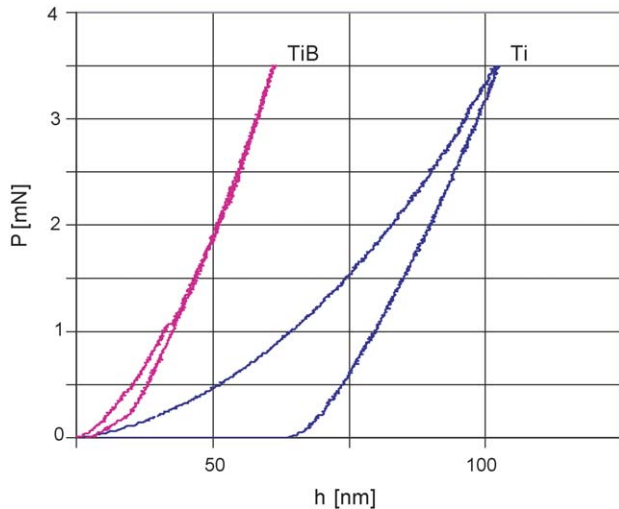
Fig. 5. Typical $P - h$ responses of indentations on Ti and TiB. Indents span within this range depending on the degree of ineteraction between the two phases.

in elasto-plastic indentation characterized by a residual indentation depth h_f:

$$h_c - h_f = \frac{2}{\pi}(h_{max} - h_f) \tag{17}$$

Since h_{max} and h_f are measurable quantities, one can determine the contact depth h_c from Eq. (17), and subsequently the contact area $A_c = \mathcal{A}(h_c)$, where $\mathcal{A}(h_c)$ is a polynomial function describing the imperfect indenter tip geometry and is calibrated by performing several indents on specimen with known properties (here, fused silica) [30]. In practice, however, the residual indentation depth h_f is very sensitive to surface imperfections. For purely elastic unloading with a conical indenter geometry, the $P - h$ response follows the quadratic form of the loading regime:

$$P = c(h - h_f)^2; \qquad h - h_f = 2\frac{P}{S} \tag{18}$$

such that the magnitude of h_f is not required. Indeed, a combination of Eqs. (17) and (18) yields:

$$\frac{h_c}{h_{max}} = 1 - \epsilon\frac{P_{max}}{Sh_{max}} \tag{19}$$

where $\epsilon = 2(1 - 2/\pi) = 0.73$. Eq. (19) is also valid for other indenter shapes: $\epsilon = 1$ for a flat punch, and $\epsilon = 0.75$ for a parabola of revolution. The main assumption incorporated in this analysis is that the surface area beyond the contact points conforms with the elasticity solutions: it assumes that the material sinks-in. The main assumption of the Oliver and Pharr method is that the shape of the deformed solid outside the area of contact is elastic. This is not true when plastic deformations occur around the indenter to form material pile-up. Indeed, Eq. (19) cannot predict $h_c/h > 1$ which may be the source of important errors. The second concern about this method is that most of the unloading curves in Berkovich indentation tests obey to a power relation of the form:
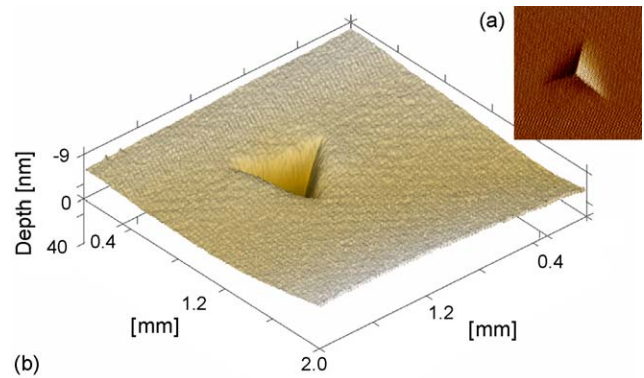
$$P = c(h - h_f)^m \tag{20}$$

Fig. 6. An atomic resolution scanning probe microcopy image of a residual indent on a Ti–TiB–TiB$_2$ specimen in (a) gradient and (b) three-dimensional rendering.

with values for the power-law exponent in the range $1.2 \le m \le 1.6$ for a large range of tested materials [31]. By comparing this experimental scaling relation with the closed form elastic solutions for the flat punch ($P \propto h$), conical indenter ($P \propto h^2$) and paraboloid of revolutions ($P \propto h^{3/2}$) [36], it appeared that the unloading curves are best approximated by an indenter that behaves like a paraboloid of revolution, ($m = 1.5$); and the value $\epsilon = 0.75$ was recommended for Berkovich indentation. The conclusions are somewhat surprising because the axi-symmetric equivalent of the Berkovich indenter is a cone, for which $m = 2$. This discrepancy has since been explained by the concept of an "effective indenter shape" [31]: During loading the localized area around the indent gets heavily distorted and as a consequence, upon unloading, permanent deformations remain on the surface of the material. Reloading that region involves a conical surface that pushes against a concave surface. According to Oliver and Pharr, such a phenomenon can be well approximated by a paraboloid indenter pressed against a flat surface.

Detailed finite element simulations and experiments (see Refs. [31,30] and references therein) have shown that Eq. (19) is in very good agreement with the actual area of contact at maximum load, provided that there is no significant pile-up of material at the contact perimeter. Scanning probe microscopy images of residual indentations (Fig. 6) demonstrate that there is no visible pile-up in the Berkovich indentation of the Ti–TiB composites, suggesting that the Oliver and Pharr method would yield reliable estimates of the area of contact. The large amount of analyzed indentation data was then treated in a statistical fashion.

4.2.1. Mechanical response distributions

Mechanical response distributions represented as frequency plots are used to analyze indentation data on a composite material. For small indentation depths, $h \ll D$, such plots give rise to multimode distributions, each peak corresponding to the mechanical manifestation of a phase.[2] In order to extract elastic properties of the relevant phases, the deconvolution technique

---

[2] In the case of nanoindentation on Ti–TiB systems, the mechanical phases coincide with a chemical phase. Such a scenario provides a direct link between physical chemistry and mechanics.
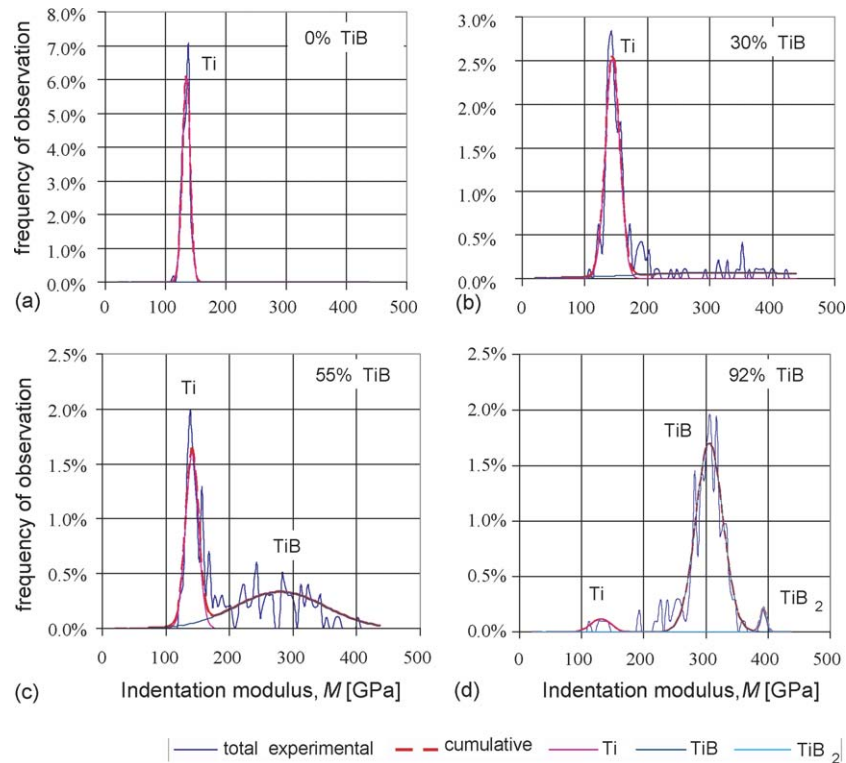
Fig. 7. Frequency plots of the indentation modulus for the four specimens: 100%Ti, 70%Ti–30%TiB, 45%Ti–55%TiB, and 92%TiB–8%TiB$_2$.

presented in Section 3.2 is employed. It should be noted, however, that this process, as is true of most optimization schemes, can result in convergence of the solution to local minima. To overcome this problem, judicious choice of the initial values of optimized parameters (using the frequency distributions) is required.

Fig. 7(a) shows the distribution of indentation modulus on a pure titanium matrix, 100%Ti. In this case, $n = 1$ and the data can be fitted by a normal distribution of the form (8), where the mean value and the standard deviation are $M_{100\%Ti} = 134 \pm 5$ GPa (see Eq. (9)). The resulting frequency plot shows a relatively small scatter and high repeatability, underscoring the microstructural and mechanical homogeneity of this elemental matrix and the robustness of the indentation experiments and analysis. Fig. 7 (b)–(d) depict the frequency plots of the M for three Ti–TiB alloys; 70%Ti–30%TiB, 45%Ti–55%TiB, 92%TiB–8%TiB$_2$. It is evident from the results that a second peak increases in intensity as the boron content increases, indicating the presence of a new phase, TiB. In the case of 92%TiB–8%TiB$_2$ a small percentage of residual, unreacted TiB$_2$ remained in the matrix. This was detected by our indentation results and

is manifested as a peak in the frequency plot of Fig. 7(d) with an indentation modulus of: $M_{TiB_2} = 394 \pm 13$. The extracted indentation moduli and volumetric proportions of the different phases are summarized in Table 3. In order to quantify the effect of the phases surrounding the RVE of indentation on the calculated M of each phase, we will use as reference for M_{Ti} and M_{TiB} the results obtained on 100% Ti and 92%TiB–8%TiB$_2$ specimens accordingly. The indentation moduli obtained for Ti and TiB in the two intermediate-volume specimens, Ti–30%TiB ($M_{Ti} = 144 \pm 12$ GPa, $M_{TiB} = 330 \pm 147$ GPa) and Ti–54%TiB ($M_{Ti} = 141 \pm 10$ GPa, $M_{TiB} = 280 \pm 70$ GPa) are within 10% of the independently measured values on $M_{100\%Ti} = 134 \pm 5$ GPa and $M_{92\%TiB-8\%TiB_2} = 306 \pm 22$ GPa. This is in line with the restrictions posed by finite element calculations for the specific choice of indentation depth (see Fig. 2). Furthermore, this agreement with independent measures or computationally simulated estimates of M (see Section 4.3) for these phases supports the accuracy of the current approach in composite analysis. That is, given a reasonable choice of the indentation depth and a large number of well-designed indentation experiments, the intrinsic elastic properties of individual phases can

Table 3
Indentation moduli and volumetric proportions of the different phases (Ti and TiB) obtained from the deconvolution of the experimentally obtained frequency plots

	Indentation Modulus, M [GPa]			Volume Fraction, f [%]		
	Ti	TiB	TiB$_2$	Ti	TiB	TiB$_2$
100Ti	134 ± 5	–	–	100	0	0
70Ti–30TiB	144 ± 12	330 ± 147	–	74	26	0
46Ti–54TiB	141 ± 10	280 ± 70	–	44	56	0
92TiB–8TiB$_2$	136 ± 15	306 ± 22	394 ± 13	4	93	3

be extracted. This is a consequence of the choice of the indentation depth h, which was deliberately chosen to be small enough compared to the characteristic length of the heterogeneities D, such that an indentation test that is situated on an inclusion phase satisfies $h/D \ll 1$.

The relatively high standard deviation observed for the TiB phase should be noted. This is a consequence of the " substrate effect" due to proximity of non-TiB phases in close proximity to the RVE that includes TiB. Since the whisker width varies significantly, the condition $h/D \ll 1$ is likely violated in a significant number of individual experiments within the massive array. In principle, this experimental obstacle could be overcome by further reducing the maximum indentation depth, but was beyond the limits of the current experimental capabilities due to geometric imperfections at the indenter apex for $h < 40$ nm. The proximity effect is also demonstrated by the decrease in the standard deviation with increasing volumetric proportions of TiB. It has been shown that the characteristic size of the TiB, D, increases in the case of 92%TiB–8%TiB$_2$ (see Ref. [1] and Section 4.1.2), and thus the condition h/D is better satisfied as f_{TiB} increases.

4.2.2. Volumetric proportions

The volumetric proportions of the two phases, Ti and TiB, have been measured by quantitative X-ray diffraction analysis and are reported in Table 1 (see also Ref. [34]). The direct comparison method [10], used extensively to estimate the retained austenite in hardened steels, was here used to provide an estimate of the TiB volume fractions in various composites. In this method, the volume fractions are determined from the relative intensities of a particular plane (preferably the strongest reflection) of TiB phase relatively to the integrated intensity of the strongest TiB line. Accordingly, the volume fraction of TiB (V_f) can be written as:

$$V_f = \frac{R_{Ti} I_{TiB}}{R_{Ti} I_{TiB} + R_{TiB} I_{Ti}} \tag{21}$$

where I is the integrated intensity of the $(h\,k\,l)$ peak. The parameter R is given by:

$$R = \frac{|F_{hkl}|^2 pL}{V_0} \tag{22}$$

where V_0 is the volume of unit cell, F_{hkl} is the structure factor, p is the multiplicity factor, and L is the Lorentz polarization factor. The reflections used in the analysis were $(1\,0\,1)$Ti, $(2\,0\,0)$TiB and $(1\,0\,1)$TiB$_2$.

An estimate of the volumetric proportions of the different phases is also given by the relative area of each individual Gaussian distribution under the cumulative frequency plot (see Section 3.2 and Eq. (10)). The resulting values after deconvoluting the four alloys are provided in Table 3, and demonstrate the capacity of grid indentation to quantify the relative presence of different phases. Importantly, herein these volume fractions are determined not by the differential chemical composition of these phases, but by the differential mechanical properties of these phases. It should be noted that this criterion immediately implies that the volume fractions estimated by the indentation

approach increase in accuracy as the mechanical dissimilarity between any two phases increases.

4.2.3. Mechanical mapping of microstructure

Instrumented indentation facilitates controlled spatial distribution among indents in patterns such as regularly spaced arrays. In the nanoindentation arrays employed herein, a square grid of 10 μm inter-indentation spacing was chosen. The analysis of each indentation $P - h$ response provides information about the mechanical properties such as M at each array coordinate (x, y). These properties are, strictly speaking, representative of a material domain of characteristic length scale $\max(h, a)$ that defines the RVE. Hence, provided that the array spacing is larger than the characteristic length scale of the material sampled in each experiment, mapping of the properties over the grid region indicates the morphological arrangement of the phases comprising the microstructure. A convenient and simple way to generate these maps is by transforming the discrete data system into a continuous distribution of mechanical properties by linearly interpolating the grid point values over the grid region. The result of this mapping can be displayed as contour plots in plan view (see Fig. 8). Such a contour depiction of mechani-
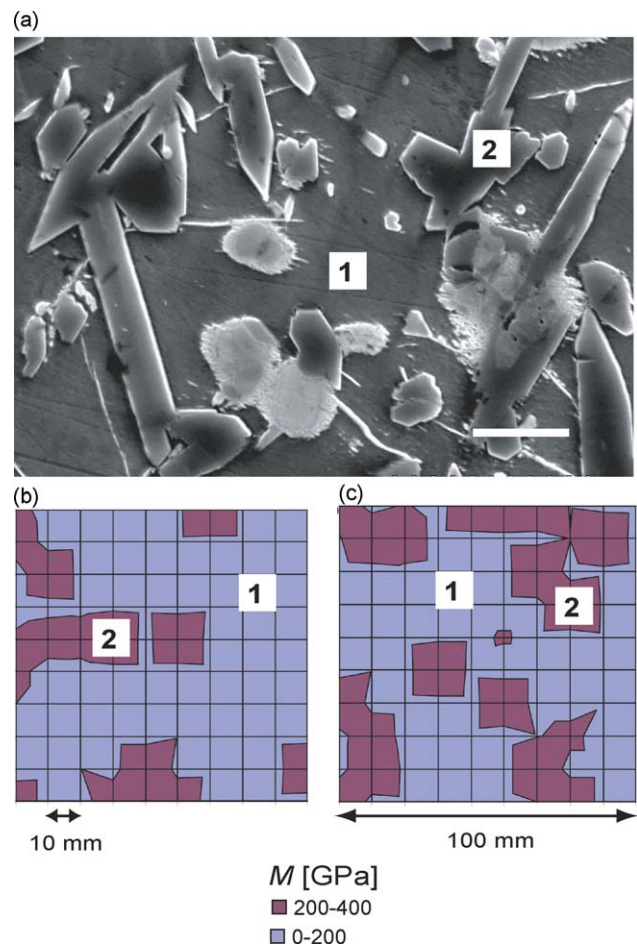

Fig. 8. Mechanical mapping of the indentation results on 70Ti–30TiB (b-c) as compared with an SEM image (a) of an etched microstructure at a similar magnification. 1 = Titanium (Ti), 2 = Titanium monoboride (TiB). Scalebar = 10 μm.

cal properties requires the selection of minima-maxima limits between different phases. As the frequency plots in Figs. 7(b) to (d) show, there is some overlap in the distribution between different phases, which complicates the definition of clear boundaries between phases. As a first-order approach, we choose equal size domains centered around the mean values of each phase:

1. 0–200 GPa: Values situated in this range are associated with regions for which the mechanical response is dominated by the titanium matrix.
2. 200–400 GPa: Values situated in this range are contained within the second peak in the frequency plots of Figs. 7(b) to (d), and are associated with regions in which the mechanical response is dominated by the TiB whiskers.

Fig. 8 shows plan views of contour plots of the indentation modulus for the Ti–30%TiB specimen. An SEM image is also shown in Fig. 8, and demonstrates the correlation of these mechanical maps with electron microscopy images of the microstructure. Hence, the mechanical maps provide a means to characterize the morphology of the microstructure at the scale defined by the chosen indentation depth, and enables visualization of the mechanically distinct features. In particular, for the Ti–TiB composite, the contour plots provide a snapshot of the formation process of the composite: TiB whiskers and particles are embedded in a percolated matrix of Ti (see Fig. 8). The morphological characterization of the microstructure provided by this mechanical mapping completes the characterization of the properties and morphological arrangement in space. As it will be further discussed in Section 4.3.2, these data are a piece of the puzzle for the development of micromechanical models for upscaling of composite mechanical performance [43].

4.3. Elastic properties of Ti, TiB, and TiB$_2$

The indentation moduli M determined from the grid indentation experiments for the Ti, TiB, and TiB$_2$ phases are insensitive to spatial location, number of experiments, and specimen preparation procedure. The extracted values can therefore be considered as mechanical properties characteristic of each phase. To further investigate the intrinsic nature of these properties, we compare our results with values reported in the literature. Since the TiB phase cannot be reproduced in macroscale physical dimensions, data on the elastic constants of this phase are scarce. In fact, the only information regarding E of this phase is provided by atomistic simulations [18] or by extrapolating macroscopic experiments on composites comprising different volumetric proportions of TiB, f_{TiB}, to $f_{TiB} = 1$ [1].

4.3.1. Elastic modulus in terms of M
Elastic contact mechanics provides a convenient framework for linking the measured indentation modulus, M, with the elastic properties of the indented material. The Galin-Sneddon solution [15,20,27,33,36–38] of a rigid, axisymmetric indenter acting on a linear elastic, isotropic, infinite half-space suggests that the

indentation modulus is directly related to the Young's modulus, E, and Poisson's ratio, ν, of the indented material:

$$M_s = M = \frac{E_s}{(1 - \nu_s^2)} \tag{23}$$

where the subscript s indicates the indented material, $s =$ Ti, TiB, TiB$_2$. The effect of indenter compliance can be considered by substituting for M in Eq. (23) the commonly employed [6,17,31] result of the Hertz contact solution of two elastically deformable bodies [21]:

$$\frac{1}{M} = \frac{1 - \nu^2}{E} + \frac{1 - \nu_{in}^2}{E_{in}} \tag{24}$$

where E, ν and E_{in}, ν_{in} are the elastic constants of the indented material and the indenter, respectively. Strictly speaking, diamond crystals are transversely isotropic and Eq. (24) is only approximate. The International Standards Organization has recently issued a draft international standard (ISO 14577-2002, [23]) in which recommend the use of $E_{in} = 1140$ GPa, $\nu_{in} = 0.07$ for diamond indenters. For the purposes of our analysis, we will therefore employ these proposed isotropic constants.

The indentation moduli can be converted to the elastic properties of the individual phases by considering Eq. (24) and assuming a Poisson's ratio for each phase. It is interesting to decompose the effect of the indenter deformation and the Poisson's effect on the magnitude of E calculated from a given M. To this end, we start by calculating the material plane-stress elastic modulus M_s, which does not include any assumption on the Poisson's ratio. Fig. 9 shows the contribution of the indenter deformation on the elastic properties extracted thereby. The horizontal axis corresponds to the measured (composite) M which implicitly includes the deformation of the indenter, and the vertical axis quantifies the effect of indenter deformation on M_s calculated as a function of M for a given indenter stiffness. It is impressive to note that as the stiffness of the indented material increases, the indenter deformation becomes more significant and should be accounted in our analysis. In
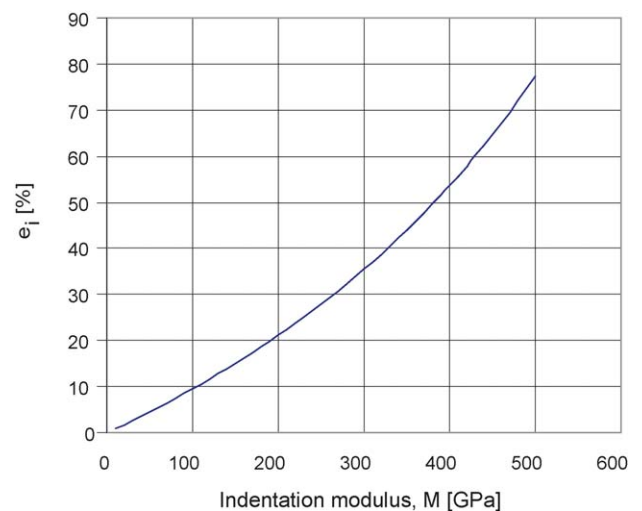

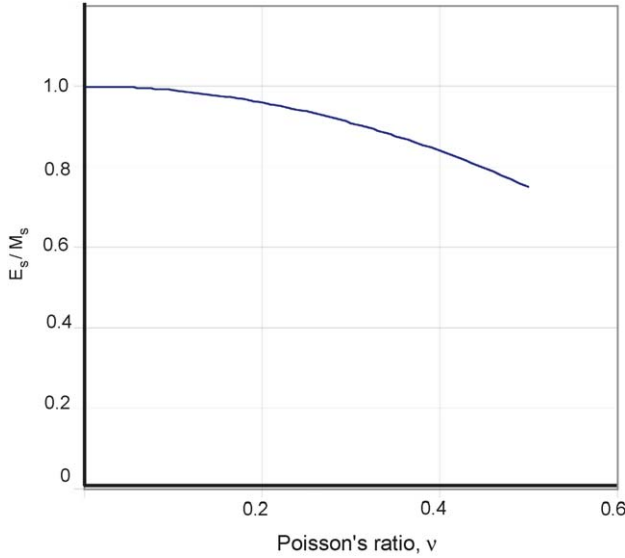Fig. 9. Error induced by the deformation of the indenter, defined as $(M_s - M)/M \times 100$.

Fig. 10. Sensitivity of the dimensionless ratio of Young's modulus normalized by indentation modulus, E_s/M_s, to the Poisson's ratio ν_s, over the range of commonly observed values of ν for engineering materials: $0 \leq \nu \leq 0.5$.

the following calculations, we will rely on the Hertz solution of the contact between two isotropic solids of Eq. (24), and the isotropic assumption of the diamond indenter suggested by ISO [23].

Given the plain-stress elastic modulus of the indented material, the Young's or uniaxial elastic modulus, $E_s = M_s \times (1 - \nu^2)$ can be determined, provided a reasonable estimate of the Poisson's ratio. However, it is not necessary to know the value of the Poisson's ratio with great precision to obtain a reasonable estimate of the Young's modulus. In fact, a Poisson's ratio of 0.1–0.4, representative of the range including most engineering metals and ceramics, induces an error on E of less than 10% (see Fig. 10). Assuming a value of $\nu = 0.32$ [13], 0.16 [1], 0.17 [29] for Ti, TiB, and TiB_2, respectively, the elastic moduli of the three phases can be calculated:

$$M = \begin{cases} M & M_s & (M_s - M)/M_s & E_s & \\ [\text{GPa}] & [\text{GPa}] & [\%] & [\text{GPa}] & \\ 140 & 159 & 14 & 138 & \text{Ti} \\ 305 & 416 & 36 & 406 & \text{TiB} \\ 394 & 600 & 52 & 585 & TiB_2 \end{cases}$$

The elastic moduli of Ti and TiB ($E_{\text{Ti}} = 138$ GPa, $E_{TiB_2} = 585$ GPa) are in excellent agreement with macroscopic properties reported in the literature: $E_{\text{Ti}}^{\text{lit}} = 110–120$ GPa [13], $E_{TiB_2}^{\text{lit}} = 565$ GPa [29]. The elastic properties of the TiB, however, remain a matter of current debate. This material exhibits crystalline anisotropy (orthorhombic unit cell), but the nine elastic constants required to describe the stiffness tensor have never been measured experimentally, chiefly due to the inability to prepare appropriate samples. Estimates of E_{TiB} that assume isotropic behavior vary widely ($E_{\text{TiB}}^{\text{lit}} = 232–622$ GPa). A value of $E_{\text{TiB}}^{\text{lit}} = 371$ GPa was suggested from inverse analysis of the composite elastic modulus [1], whereas a value of $E_{\text{TiB}}^{\text{lit}} = 485$ GPa was estimated from *ab-initio* atomistic simulations [18]. Some esti-

mates from indentation experiments have also been reported [18], but the experimental scatter was quite significant. Thus, validation of the magnitude of E_{TiB} obtained herein by recourse to existing data is difficult.

4.3.2. Micromechanical modeling and macroscopic composite behavior

To investigate the accuracy of our extracted E_{TiB}, we will use $E_{\text{TiB}}^{\text{exp}} = 406$ GPa as input in a composite model that predicts the macroscopic (homogenized) response, and compare this prediction with reported macroscopic data. The Ti–TiB composite can be conveniently modeled with the Mori-Tanaka micromechanical scheme, which is suitably applied for matrix-inclusion geometries [28]. The model has been tested on several materials and has been found to show very good predictive capabilities (see e.g., Ref. [7]). In the case of a titanium matrix with isotropic spherical inclusions of TiB, the Mori-Tanaka scheme yields the following homogenized response ($K_{\text{hom}}, G_{\text{hom}}$):

$$K_{\text{hom}} = K_{\text{Ti}} + \frac{(K_{\text{TiB}} - K_{\text{Ti}})f_{\text{TiB}}}{1 + a(1 - f_{\text{TiB}})((K_{\text{TiB}}/K_{\text{Ti}}) - 1)} \quad (25)$$

$$G_{\text{hom}} = G_{\text{Ti}} + \frac{(G_{\text{TiB}} - G_{\text{Ti}})f_{\text{TiB}}}{1 + b(1 - f_{\text{TiB}})((G_{\text{TiB}}/G_{\text{Ti}}) - 1)} \quad (26)$$

where K_{Ti} and K_{TiB} are the bulk modulus of the titanium matrix and TiB inclusion, respectively, and G_{Ti} and G_{TiB} are the shear modulus of the titanium matrix and titanium boride inclusion, respectively. The variables a and b in Eqs. (25) and (26) are stated as:

$$a = \frac{3K_{\text{Ti}}}{3K_{\text{Ti}} + 4G_{\text{Ti}}}; \qquad b = \frac{6}{5}\frac{K_{\text{Ti}} + 2G_{\text{Ti}}}{3K_{\text{Ti}} + 4G_{\text{Ti}}} \quad (27)$$

Eqs. (25) and (26) simplify the elongated whisker morphology of the titanium composite by equivalent isotropic spheres. It has been found however that, given the random orientation of the fibers in the matrix, the experimentally observed isotropic behavior of a macroscopic composite can be well approximated by a spherical assumption [1,7]. Finally, given the homogenized values of the bulk and shear moduli, the Young's modulus and the Poisson's ratio can be calculated using standard relations of elasticity theory:

$$E_{\text{hom}} = \frac{9K_{\text{hom}}G_{\text{hom}}}{3K_{\text{hom}} + G_{\text{hom}}}; \quad (28)$$

$$\nu_{\text{hom}} = \frac{3K_{\text{hom}} - 2G_{\text{hom}}}{6K_{\text{hom}} + 2G_{\text{hom}}} \quad (29)$$

The mean elastic values of titanium boride ($E_{\text{TiB}} = 406$ GPa, $\nu_{\text{TiB}} = 0.16$), as extracted from the indentation analysis (see Table 3), are incorporated in Eqs. (25) and (26) to calculate the micromechanical predictions of E for a series of f_{TiB}. A mean value between our indentation estimate and literature values is used for the elastic properties of the titanium matrix ($E_{\text{Ti}}^{\text{lit}} = 120$ GPa, $\nu_{\text{TiB}} = 0.32$). The micromechanical predictions of the E and G, together with experimental data found in the literature (Refs. [1,13,18]), are reported in Fig. 11. The impressive accuracy of the predictions validates the extracted elastic
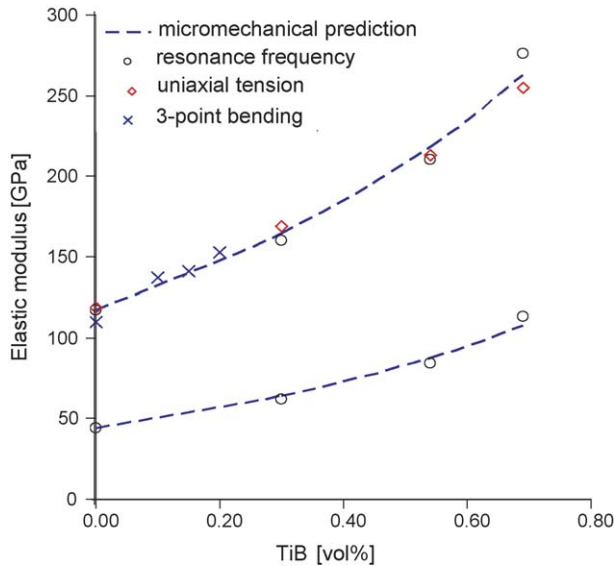
Fig. 11. Experimental data and micromechanical predictions of composite modulus (Upper: Young's modulus E; Lower: Shear modulus G) versus the volume fractions of the reinforcing TiB. Source of Macroscopic data: Resonance Frequency [1]; Uniaxial Tension [1]; 3 Point Bending [18].

modulus of the TiB phase, as well as the use of the Mori-Tanaka scheme to capture the strain localization within TiB inclusions.

This verification of E_{TiB} completes the validation of the proposed massive array or grid indentation approach. This methodology is of particular importance for materials for which the properties of constituent phases are measurable only *in situ*. As such, grid indentation represents the only currently available approach for measuring the intrinsic mechanical properties of phases as required for micromechanical modeling of composite response.

5. Conclusions

1. The proposed massive array indentation approach can provide the *in situ* elastic properties of individual phases within a multiphase microstructure. The proposed methodology relies on careful choice of the indentation depth and on a large number of experiments that are treated in a simple statistical manner. This provides a framework to determine valuable information about the composite microstructure, including the morphological arrangement and volumetric proportions of each mechanically dissimilar phase.
2. In cases for which the elastic properties of the indented material are comparable to the elastic properties of the indenter ($M > 100$ GPa), error is minimized by including the contribution of the indenter elastic deformation. In our calculation the indentation deformation was evaluated using the commonly employed model of Hertz. A more detailed analysis that takes the anisotropic behavior of the indenter into account requires further attention.
3. Application of this approach in a titanium-titanium boride binary alloy system yielded an average value for Ti, TiB, and TiB$_2$ of $E_{\text{Ti}} = 138$ GPa, $E_{\text{TiB}} = 406$ GPa, and $E_{\text{TiB}_2} =$

585 GPa. These magnitudes of E assume the isotropic nature of all phases, and are in agreement with available literature values. Further, by employing the phase properties so obtained, the elastic modulus of each Ti–TiB composite predicted by micromechanical modeling agrees well with that obtained through independent experiments, suggesting that such a simplified micromechanical approach can be conveniently employed for modeling purposes.

References

[1] R.R. Atri, K.S. Ravichandran, S.K. Jha, Mater. Sci. Eng. A 271 (1999) 150.
[2] S.I. Bulychev, V.P. Alekhin, M.K. Shorshorov, A.P. Ternovskii, G.D. Shnyrev, Ind. Lab. (Transl: Zavodskaya Laboratoria) 41 (1975) 1409 cited from [3].
[3] F.M. Borodich, L.M. Keer, C.S. Korach, Nanotechnology 14 (2003) 803.
[4] H. Buckle, in: J.W. Westbrook, H. Conrad (Eds.), The Science of Hardness Testing and Its Applications, American Society for Metals, Metal Park OH, 1973, pp. 453–459.
[5] X. Chen, J.J. Vlassak, J. Mater. Res. 16 (2001) 2974.
[6] Y.T. Cheng, C.M. Cheng, Mater. Sci. Eng. R44 (2004) 91.
[7] R.M. Christensen, J. Mech. Phys. Solids 38 (1990) 379.
[8] G. Constantinides, F.-J. Ulm, K.J. Van Vliet, Mat. Struct. 205 (2003) 191 (Special issue of Conrete Sci Eng).
[9] G. Constantinides, F.-J. Ulm, Cement Concrete Res. 34 (2004) 67.
[10] B.D. Cullity, Elements of X-ray Diffraction, second ed., Addison Wesley Inc, Reading, MA, 1978.
[11] M. Dao, N. Chollacoop, K.J. Van Vliet, T.A. Venkatesh, S. Suresh, Acta Mater. 49 (2001) 3899.
[12] K. Durst, M. Goken, H. Vehoff, J. Mater. Res. 19 (2004) 85.
[13] A. Evans, C. San Marchi, A. Mortensen, Metal Matrix Composites. An Introduction and a Survey, Kluwer Academic Publisher, 2003.
[14] A.C. Fischer-Cripps, Nanoindentation, Springer Verlag, New-York, 2003.
[15] L.A. Galin, translated by H. Moss. in: I.N. Sneddon (Ed.), Contact Problems in Theory of Elasticity, North Carolina State College, 1951.
[16] H.J. Gao, C.H. Chiu, J. Lee, Int. J. Solids Struct. 29 (1992) 2471.
[17] A.E. Giannakopoulos, S. Suresh, Scripta Mater. 40 (1999) 1191.
[18] S. Gorsse, Y. Le Petitcorps, S. Matar, F. Rebillat, Mater. Sci. Eng. A 340 (2003) 80.
[19] J.R. Gregory, S.M. Spearing, Compos. Sci. Technol. 65 (2005) 595.
[20] J.W. Harding, I.N. Sneddon, Proc. Cambridge Phil. Soc. 41 (1945) 16.
[21] H. Hertz, 'On the contact of elastic solids (in German), zeitschrift fur die reine und angewandte mathematik', (1881) English translation in miscellaneous papers (translated by D.E. Jones and G.A. Schott), Macmillan, London, UK, 1986, pp. 156–171.
[22] Triboindenter Users Manual, Hysitron Inc., Minneapolis, MN, 2001.
[23] ISO 14577, Metallic Materials – Instrumented Indentation Test for Hardness and Materials Parameters, 2002.
[24] R.B. King, Int. J. Solids Struct. 23 (1987) 1657.
[25] B.D. Kozola, Y.L. Shen, J. Mater. Sci. 38 (2003) 901.
[26] J. Li, T.W. Chou, Int. J. Solids Struct. 34 (1997) 4463.
[27] A.E.H. Love, Quart. J. Math. 10 (1939) 161.
[28] T. Mori, K. Tanaka, Acta Metal. 21 (1973) 1605.
[29] R.G. Munro, J. Res. Natl. Inst. Stand. Technol. 105 (2000) 709.
[30] W.C. Oliver, G.M. Pharr, J. Mater. Res. 7 (1992) 1564.
[31] W.C. Oliver, G.M. Pharr, J. Mater. Res. 19 (2004) 3.
[32] A. Perriot, E. Barthel, J. Mater. Res. 19 (2004) 600.
[33] G.M. Pharr, W.C. Oliver, F.R. Brotzen, J. Mater. Res. 7 (1992) 613.
[34] S.S. Sahay, K.S. Ravichandran, R.R. Atri, B. Chen, J. Rubin, J. Mater. Res. 14 (1999) 4214.
[35] T. Saito, T. Furuta, T. Yamaguchi, in: F.H. Froes, J. Storer (Eds.), Proceedings of a Symposium Held during Materials Week, Rosemont, Illinois, 1994.

[36] I. Sneddon, Int. J. Eng. Sci. 3 (1965) 47.

[37] I. Sneddon (Ed.), Application of Integral Transforms in the Theory of Elasticity, Springer Verlag, Wien-New York, 1977.

[38] N.A. Stillwell, D. Tabor, Proc. Phys. Soc. 78 (1965) 169.

[39] S. Suresh, A.E. Giannakopoulos, J. Alcala, Acta Mater. 45 (1997) 1307.

[40] D. Tabor, The Hardness of Metals, Oxford Classical Texts in the Physical Sciences-First published, 1951.

[41] T.C.T. Ting, J. Appl. Mech. 88 (1966) 845.

[42] H.Y. Yu, S.C. Sanday, B.B. Rath, J. Mech. Phys. Solids 38 (1990) 745.

[43] A. Zaoui, J. Eng. Mech. 128 (2002) 808.